Journal of Materials Chemistry A

ROYAL SOCIETY OF CHEMISTRY

PAPER

View Article Online
View Journal | View Issue

Cite this: *J. Mater. Chem. A*, 2020, **8**, 11649

Carbon aerogels with atomic dispersion of binary iron–cobalt sites as effective oxygen catalysts for flexible zinc–air batteries†

Yang Chen,[a] Shengqiang Hu,[b] Forrest Nichols,[c] Frank Bridges,[d] Shuting Kan,[a] Ting He,*[a] Yi Zhang *[a] and Shaowei Chen *[c]

Iron single atom catalysts have emerged as one of the most active electrocatalysts towards the oxygen reduction reaction (ORR), but the unsatisfactory durability and limited activity for the oxygen evolution reaction (OER) has hampered their commercial applications in rechargeable metal–air batteries. By contrast, cobalt-based catalysts are known to afford excellent ORR stability and OER activity, due to the weak Fenton reaction and low OER Gibbs free energy. Herein, a bimetal hydrogel template is used to prepare carbon aerogels containing Fe–Co bimetal sites (NCAG/Fe–Co) as bifunctional electrocatalysts towards both ORR and OER, with enhanced activity and stability, as compared to the monometal counterparts. High-resolution transmission electron microscopy, elemental mapping and X-ray photoelectron spectroscopy measurements demonstrate homogeneous distributions of the metal centers within defected carbon lattices by coordination to nitrogen dopants. X-ray absorption spectroscopic measurements, in combination with other results, suggest the formation of FeN_3 and CoN_3 moieties on mutually orthogonal planes with a direct Fe–Co bonding interaction. Electrochemical measurements show that NCAG/Fe–Co delivers a small ORR/OER potential gap of only 0.64 V at the current density of 10 mA cm^{-2}, 60 mV lower than that (0.70 V) with commercial Pt/C and RuO_2 catalysts. When applied in a flexible Zn–air battery, the dual-metal NCAG/Fe–Co catalyst also shows a remarkable performance, with a high open-circuit voltage of 1.47 V, a maximum power density of 117 mW cm^{-2}, as well as good rechargeability and flexibility. Results from this study may offer an ingenious protocol in the design and engineering of highly efficient and durable bifunctional electrocatalysts based on dual metal-doped carbons.

Received 4th May 2020
Accepted 27th May 2020

DOI: 10.1039/d0ta04633g

rsc.li/materials-a

Introduction

The non-renewability of fossil energy and growing environmental pollution have spurred the development of sustainable energy technologies, such as fuel cells and metal–air batteries.[1–6] Of these, zinc–air batteries represent a promising energy technology for next-generation portable electronics, due to their good rechargeability and high theoretical density (1370 W h kg^{-1}),[7,8] where the device performance is largely dictated by the reversible catalysts at the cathode for oxygen reduction (ORR) and oxygen evolution reactions (OER). Platinum-based nanoparticles have been the catalysts of choice for ORR, whereas Ir and Ru-based nanoparticles for OER. Yet their high costs and low natural abundance have hindered the practical applications of the technology. Thus, development of low-cost and high-performance electrocatalysts for ORR and OER have been attracting extensive interest.[9] Recent reports have shown that atomically dispersed metals (such as Mn, Fe and Co) within nitrogen-doped carbons, exhibit excellent electrocatalytic performance towards ORR and may even surpass the corresponding nanoparticle counterparts.[10,11] In both experimental and theoretical studies, Fe single atom catalysts (SACs) have been recognized as the most active catalysts towards ORR in alkaline media. Unfortunately, for the Fe-based SACs, Fenton reaction involving the Fe center and ORR byproduct H_2O_2 produces hydroxyl and oxygen radicals, which not only affect the durability of the catalysts by changing its chemical structure, but also damage the battery devices by corroding the ion membranes.[12] Additionally, theoretical and experimental studies have shown that the Fe-based SACs performs poorly towards OER, as compared to other 3d

[a]College of Chemistry and Chemical Engineering, Central South University, Changsha, Hunan 410083, China. E-mail: heting891020@csu.edu.cn; yzhangcsu@csu.edu.cn
[b]State Key Laboratory for the Chemistry and Molecular Engineering of Medicinal Resources, College of Chemistry and Pharmacy, Guangxi Normal University, Guilin, Guangxi 541004, China
[c]Department of Chemistry and Biochemistry, University of California, 1156 High Street, Santa Cruz, California 95064, USA. E-mail: shaowei@ucsc.edu
[d]Department of Physics, University of California, 1156 High Street, Santa Cruz, California 95064, USA

† Electronic supplementary information (ESI) available: Additional experimental data. See DOI: 10.1039/d0ta04633g

transition metals, such as Co and Ni.[13] Therefore, it is critical to improve the ORR durability and OER activity of Fe SACs such that they may be used as bifunctional oxygen catalysts in rechargeable Zn–air battery. Towards this end, the incorporation of Co atomic sites into Fe SACs represents a unique strategy. First of all, the weak Fenton activity between Co and H_2O_2 is anticipated to markedly enhance the ORR stability of Fe SACs.[14,15] In addition, prior studies have shown that Co-doped carbon exhibits a low overpotential and small Tafel slope towards OER.[16] Thus, it is envisioned that atomically dispersing Co atoms into Fe-doped carbon may achieve a bimetal catalyst with excellent ORR/OER activity and enhanced durability, in comparison to the monometal counterparts.

Herein, modified gelatin hydrogels were used as 3D structural templates and precursors to synthesize N-doped carbon aerogels (NCAG/Fe–Co), whereby Fe and Co bimetal centers were atomically dispersed into the porous, defect-rich carbon matrix.[17] This was evidenced in elemental mapping and inductively coupled plasma-optical emission spectrometry (ICP-OES) measurements. X-ray photoelectron spectroscopy (XPS) measurements suggest charge transfer between the Fe and Co centers, a unique feature that facilitated the catalytic reactions.[18,19] X-ray absorption spectroscopy (XAS) measurements, together with other results, suggest the formation of FeN_3 and CoN_3 moieties on orthogonal planes with a direct Fe–Co bonding linkage. The resulting bimetal NCAG/Fe–Co nanocomposite exhibited apparent electrocatalytic activity towards both ORR and OER. Notably, the incorporation of Co significantly improved both the ORR stability and OER activity of the Fe/carbon aerogel catalysts. With the excellent bifunctional catalytic performance, the NCAG/Fe–Co nanocomposite was used as the oxygen catalyst in a flexible Zn–air battery, which exhibited a high open circuit voltage, stable power density as well as good cycling stability, a performance even superior to that based on commercial Pt/C–RuO_2 catalysts. This suggests that atomic dispersion of dual metal sites in carbon is an effective strategy to boost the performance of carbon-based electrocatalysts for practical application in energy storage and conversion.[20]

Experimental section

Chemicals

Gelatin, potassium hydroxide (KOH), iron(II) chloride tetrahydrate ($FeCl_2 \cdot 4H_2O$), cobalt(II) acetate tetrahydrate ($Co(Ac)_2 \cdot 4H_2O$), zinc(II) acetate dihydrate ($Zn(Ac)_2 \cdot 4H_2O$), acrylamide, methylene bisacrylamide, potassium persulfate, and RuO_2 were purchased from Aladdin Reagents (Shanghai, China). Polytetrafluoroethylene (PTFE, 60 wt%) was purchased from Japan DaJin. Perchloric acid ($HClO_4$), ammonium hydroxide, and ethanol were obtained from Chengdu Xiya Reagents Chemical Technology Co. Ltd. 1,10-Phenanthroline (PM) monohydrate, acetylene black, 5% Nafion solution and RuO_2 were purchased from Sigma Aldrich. Commercial Pt/C (20 wt%) was purchased from Johnson Matthey. All other reagents were of analytical grade, and ultrapure water (Milli-Q, 18.2 MΩ cm) was used throughout this study.

Characterization

XPS spectra were acquired with an ESCALAB 250Xi instrument. X-ray diffraction (XRD) measurements were carried out with a D/max 2550 X-ray Powder Diffractometer. Scanning electron microscopy (SEM) and transmission electron microscopy (TEM) images were obtained on a Hitachi S-4800 field-emission SEM and FEI Talos F200S field-emission electron microscope. Raman spectra were collected with a Via-reflex instrument at the excitation of a 532 nm laser. ICP-OES analysis was performed with a SPECTRO BLUE SOP instrument. Nitrogen adsorption–desorption isotherms were acquired with a Micromeritics ASAP 2020 surface area and porosity analyzer. XAS measurements were performed in Shanghai Synchrotron Radiation Facility in the fluorescence mode at room temperature (298 K). Voltammetric measurements were performed with an RST 5200F electrochemical workstations (Zhengzhou, China). Rotating disk electrode (RDE, Pine Research Instrument) tests were carried out at the rotation rates of 400 to 1600 rpm.

Preparation of hydrogel precursors

Experimentally, 15 mg of PM was dispersed in 125 μL of $FeCl_2 \cdot 4H_2O$ (0.2 M) by ultrasound treatment to prepare a red $Fe(PM)_3^{2+}$ solution. Similarly, 15 mg of PM was added in 125 μL of $Co(Ac)_2 \cdot 4H_2O$ (0.2 M) by ultrasound treatment to obtain an orange $Co(PM)_3^{2+}$ solution. 60 mg of gelatin, 30 mg of SiO_2, and 2.51 mL of Milli-Q water were then placed into a screw-cap vial, and mixed under magnetic stirring in a 60 °C water bath for 10 min, into which were added 125 μL of 0.2 M $Fe(PM)_3^{2+}$, 125 μL of 0.2 M $Co(PM)_3^{2+}$ and 80 μL of 1.0 M $Zn(Ac)_2$. The obtained hydrogels were subject to freezing–thawing three times, and denoted as G_{Si-Zn}/Fe@CoPM.

Preparation of NCAG/Fe–Co

The G_{Si-Zn}/Fe@CoPM hydrogels obtained above was freeze-dried overnight in vacuum, then pyrolyzed at 900 °C for 3 h in a tube furnace under a constant flow of 97% Ar + 3% H_2 at the heating rate of 5 °C min^{-1}. During this process, Zn atoms were vaporized, which formed atomic spaces to capture Fe or Co atoms. After being cooled down naturally to room temperature, the product was etched by HF to remove the SiO_2 nanoparticles, affording NCAG/Fe–Co. For comparison, two control samples, NCAG/Fe and NCAG/Co, were also prepared in the same fashion but without the addition of $Co(PM)_3^{2+}$ and $Fe(PM)_3^{2+}$, respectively, at the same total water volume of 3.56 mL.

Synthesis of polyacrylamide (PAM) hydrogel solid electrolyte

To prepare PAM hydrogel, 4 g of acrylamide was dissolved in 16 mL of Milli-Q water under vigorous magnetic stirring at room temperature, into which were then added 4 mg of methylene bisacrylamide and 10 mg of potassium persulfate. The obtained clear solution was injected into a glass plate mold and placed overnight in a 60 °C oven. The as-prepared PAM sheet was removed from the mold and dried naturally, then immersed in a mixed solution containing 6 M KOH and 0.2 M $Zn(Ac)_2$ for 48 h before use.

Electrochemical measurements

All electrochemical tests were carried out in a three-electrode configuration. To prepare the catalyst inks, 3 mg of the catalyst powders obtained above was added to a vial containing 475 μL of a H_2O and C_2H_5OH mixture (v/v = 1 : 1) and 25 μL of a Nafion solution (5%). Cyclic voltammetry (CV) measurements were carried out on an RST 5200F electrochemical workstation with a KCl-saturated Ag/AgCl electrode as the reference electrode, a Pt wire as the counter electrode and a glassy carbon disk electrode, with a catalyst loading of 0.255 mg cm^{-2}, as the working electrode. Oxygen-saturated 0.1 M KOH or 0.1 M $HClO_4$ was used as the electrolyte.

Rotating disk electrode (RDE) and rotating ring-disk electrode (RRDE) tests were carried out to assess the ORR activity with a Pine Research Instrument bipotentiostat. A KCl-saturated Ag/AgCl electrode was used as the reference electrode, a Pt plate as the counter electrode and a glassy carbon electrode at the catalyst loading of 0.425 mg cm^{-2} as the working electrode.

The OER polarization curves were acquired with an RST 5200F electrochemical workstation in a 1 M KOH electrolyte, with the KCl-saturated Ag/AgCl electrode as the reference electrode, a graphite rod as the counter electrode, and a carbon paper at the catalyst loading of 1 mg cm^{-2} as the working electrode. To prepare the working electrode, 1.5 mg of the catalysts obtained above, 2 mg of acetylene black and 1.3 μL of PTFE (60 wt%) were evenly mixed and coated on a piece of carbon paper (1.5 × 1.0 cm^2), which was then vacuum-dried for 3 h at 60 °C. The carbon paper was cut into 0.5 × 0.5 cm^2 pieces and used as the working electrode.

The Ag/AgCl electrode was calibrated against a reversible hydrogen electrode (RHE), and all potentials in the present study were referenced to this RHE.

Fabrication and testing of liquid and solid Zn–air batteries

Liquid rechargeable Zn–air batteries were assembled with a homemade cell. A zinc sheet (purity 99.9 wt%) was used as the anode, which was polished with sandpaper before use. A mixed solution of 6 M KOH and 0.2 M $Zn(Ac)_2$ was used as the electrolyte. The air cathode was composed of three layers, a catalyst layer, a nickel foam layer and a gas diffusion layer. The catalytic layer was fabricated by homogeneously mixing the NCAG/Fe–Co catalyst, acetylene black, PTFE (60 wt%) at the mass ratio of 6 : 1 : 3. The nickel foam was treated with 0.2 M HCl, water and ethanol for 20 min, successively, and then vacuum dried at 60 °C before use. The three layers were compressed with a roll press to obtain the cathode, which was then vacuum dried at 60 °C for 3 h.

Solid-state Zn–air battery with a sandwich structure was assembled by replacing the zinc sheet and liquid electrolyte with a zinc foil (purity 99.9 wt%) and the as-fabricated PAM sheet, respectively.

For comparison, Zn–air batteries were also assembled in the same manner, except that the oxygen cathode was based on the mixture of commercial Pt/C : RuO_2 catalysts (1 : 1 by mass).

In all zinc–air battery performance tests, the mass loading of the catalysts (*i.e.*, NCAG/Fe–Co, and Pt/C : RuO_2 mixture) was 1 mg cm^{-2}.

Results and discussion

Characterization and structural analysis

The synthetic procedure for the NCAG/Fe–Co carbon aerogel entails two major steps: (a) a freeze-dried hydrogel network was prepared and used as the 3D structural template, where gelatin–Zn, bimetal–PM complex and SiO_2 nanoparticles served as the sources of N-doped carbon, metal centers, and porogens, respectively; and (b) subsequent pyrolysis and acid etching led to the facile production of N-doped carbon aerogels with atomic dispersion of Fe and Co (NCAG/Fe–Co, Fig. 1a).[21] The monometal counterparts (NCAG/Fe and NCAG/Co) were prepared in the same manner. The sample structures were first examined by SEM measurements. From Fig. 1b and S1,† the freeze-dried gelatin hydrogels can be seen to exhibit a network of micron-sized pores. Upon pyrolysis and HF etching, the resulting NCAG/Fe–Co aerogels contained abundant mesopores (Fig. 1c). From the HRTEM image in Fig. 1d, one can see a highly disordered carbon structure and plentiful mesopores, and a number of metal atoms were randomly distributed in the carbon lattices (marked by red cycles). Note that no nanoparticle or nanocluster species were found. Elemental mapping analysis (Fig. 1e) shows that the distinct signals of N, O and C were distributed evenly across the entire carbon matrix, whereas those for Fe and Co were rather scattered. These results suggest the successful production of dual metals and N doped carbon aerogels from a hydrogel template/precursor.

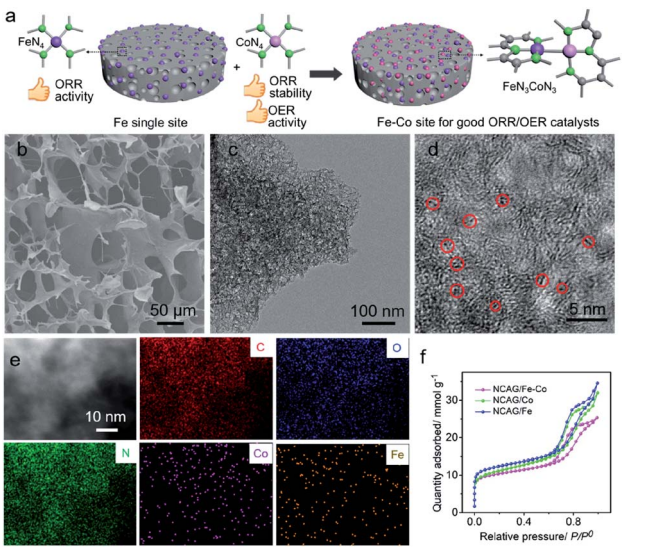

Fig. 1 (a) Schematic illustration of the combination of Fe and Co single atom catalysts into Fe–Co dual metal-doped carbon aerogel. (b) SEM image of the freeze-dried G_{Si-Zn}/Fe@CoPM hydrogel. (c) TEM image of the NCAG/Fe–Co aerogel. (d) HRTEM image of the NCAG/Fe–Co aerogel. The red circles indicate metal clusters. (e) HAADF-STEM image and elemental maps of NCAG/Fe–Co. (f) Nitrogen adsorption–desorption isotherms of NCAG/Fe–Co, NCAG/Fe, and NCAG/Co.

N_2 absorption–desorption isotherms were then acquired to investigate the porosity of the obtained nanocomposites (Fig. 1f). Table S1† lists the calculated specific surface areas and pore volumes. One can see that all samples are mainly composed of micropores and mesopores (Fig. S2†) with a close surface area ranging from 748.2 to 893.3 $m^2 g^{-1}$, a feature that is conducive for mass transfer during catalytic reactions. Of note is that NCAG/Fe–Co displays the largest fraction of micropores (32.1%), suggestive of rich edge defects for capturing individual metal atoms.[22]

Further structural insights were obtained in XRD and Raman measurements. From Fig. 2a, all three samples can be seen to show only a broad peak between $2\theta = 20°$ and 30°, which is attributed to the (002) plane of graphitic carbon (PDF 656212). Notably the peak position varies slightly among the three NCAG samples, at $2\theta = 23.9°$ for NCAG/Fe, 24.6° for NCAG/Fe–Co and 25.5° for NCAG/Co, with the corresponding interplanar spacing of 3.7 Å, 3.6 Å and 3.5 Å, respectively. Note that no other diffraction patterns can be resolved, consistent with the absence of metal (oxide) nanoparticles in the samples (Fig. 1c and d). Successful graphitization of the hydrogels by pyrolysis is also evidenced in Raman measurements (Fig. 2b), where all samples exhibited a well-defined D band (sp^2 hybrid carbon) at 1347 cm^{-1} and G band (sp^3 hybrid carbon) at 1595 cm^{-1}, with a low D band to G band intensity ratio ($I_{D/G}$) at 0.83, 0.89, and 0.77, respectively.

The elemental compositions were then analyzed by ICP-OES and XPS measurements. The results of the ICP-OES measurements are summarized in Table S2,† where the total metal content is estimated to be 0.6 wt% for NCAG/Fe, 1.0 wt% for NCAG/Co, and 1.8 wt% for NCAG/Fe–Co (including 0.7 wt% Fe and 1.1 wt% Co). XPS measurements show that the carbon aerogels consisted of *ca.* 89 wt% C, 5 wt% O, 5 wt% N and 1 wt% metals (Table S3†), in good agreement with the ICP-OES results. Note that in comparison with NCAG/Fe, NCAG/Fe–Co and NCAG/Co exhibit a slightly higher content of N and lower content of O, suggesting a higher degree of graphitization by Co, which may facilitate electron transfer during electrocatalytic reactions. The high-resolution scan of the N 1s electrons are depicted in Fig. 2c and S3.† From deconvolution, one can see that the majority of the N species in the carbon aerogels is graphitic N, with a minority of metal N (M–N) and pyridinic N. As listed in Table S4,† the M–N species in NCAG/Fe–Co is 1.4 wt%, much higher than those of NCAG/Fe (0.8 wt%) and NCAG/Co (1.0 wt%). Intriguingly, the ratio between N in M–N species (1.5 at%) and the metal content (0.5 at%) in NCAG/Fe–Co is about 3 : 1, suggesting the formation of MN_3 coordination moieties in the sample.

Furthermore, from Table S4,† the N 1s binding energy of M–N in NCAG/Fe–Co (398.9 eV) can be seen to be *ca.* 0.1 eV higher than that of NCAG/Fe (389.8 eV), but 0.1 eV lower than that of NCAG/Co (399.0 eV), consistent with the higher electron affinity of cobalt than that of iron. Based on the binding energy of the metal 2p electrons (M = Fe or Co), M(II/III) turns out to be the predominant species in these carbon aerogels (Fig. 2d and S4†). In comparison to NCAG/Fe, the binding energy of Fe(II) and Fe(III) for NCAG/Fe–Co show a positive shift of +0.5 eV and +0.3 eV, respectively (Table S5†). On the contrary, the binding energy of Co(II) for this dual-metal catalyst shows a negative shift of 0.2 eV, compared to that of NCAG/Co. These variations in binding energy suggest electron transfer from the Fe to Co sites in NCAG/Fe–Co. It has been known that the poor durability of Fe-based ORR catalysts is mainly due to the Fenton reaction, where the Fe(II) centers act as the reductant. The reduced electron density of the Fe centers in NCAG/Fe–Co observed above may therefore hinder the Fenton reaction, and enhance the ORR durability, as observed below in electrochemical measurements.

XAS measurements were then conducted to investigate the chemical states and coordination configurations of the metal atoms in the aerogel catalysts. From Fig. 3a, one can see that the Fe K-edge X-ray absorption near-edge structure (XANES) spectrum of the dual-metal NCAG/Fe–Co catalyst resembles that of FePc, but is apparently different from that of the Fe foil. This indicates that the valence state of Fe in NCAG/Fe–Co is close to +2, in good agreement with results from XPS measurements (Table S5†).

The corresponding extended X-ray absorption fine structure (EXAFS) spectra at the Fe K edge are depicted in Fig. 3b. To construct a starting structure, we use two results obtained above: (i) the relative atomic fractions of N to metals is 3 : 1, suggesting the formation of MN_3 moieties, and (ii) the apparent change in binding energies for Fe when Co is present suggests charge transfer between Fe and Co and hence pairing of Fe and Co atoms in a fairly close proximity. This leads to a structure similar to that in Fig. 1a. The first broad peak at about 1.5 Å can be observed for both FePc and NCAG/Fe–Co (Fig. 3b, S5 and Table S6†), which is ascribed to the nearest Fe–N coordination; this indicates a Fe–N bond length close to 2 Å (note that there is

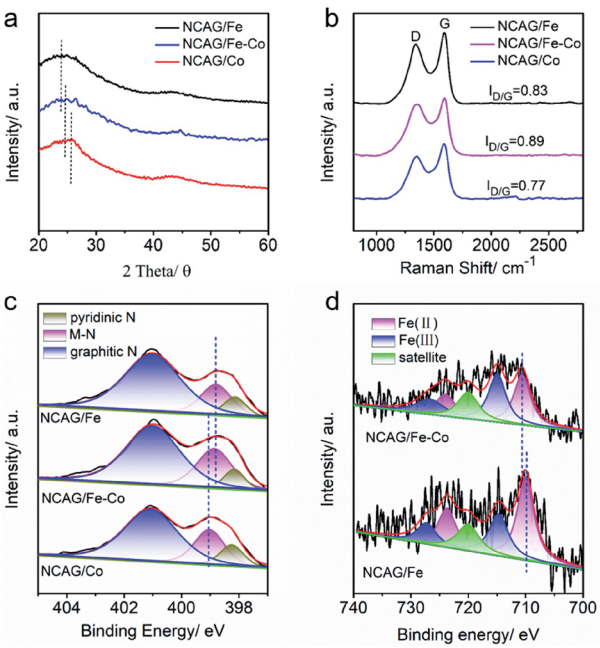

Fig. 2 (a) XRD patterns of NCAG/Fe–Co, NCAG/Fe, and NCAG/Co. (b) Raman spectra of NCAG/Fe–Co, NCAG/Fe, and NCAG/Co. (c) High-resolution XPS spectra of the N 1s electrons in NCAG/Fe–Co, NCAG/Fe, and NCAG/Co. (d) High-resolution XPS scan of the Fe 2p electrons in NCAG/Fe–Co, and NCAG/Fe.

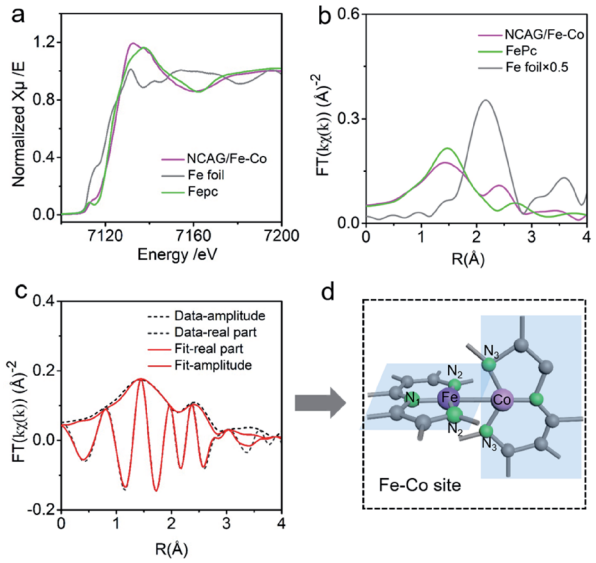

Fig. 3 (a) Fe K-edge XANES and (b) EXAFS of NCAG/Fe–Co, Fe foil and FePc. (c). Fe K-edge EXAFS of NCAG/Fe–Co and the fitting curve. (d) Schematic illustration of the structure of the Fe–Co dual metal sites in NCAG/Fe–Co.

a well-known and calculable phase shift in EXAFS that shifts the peaks of an EXAFS profile to a shorter *R*). However this peak is unusually broad and has a significant shoulder near 1.9 Å, suggestive of another Fe–N peak near 2.4 Å.

The second well-defined peak at 2.4 Å is attributed to a Fe–M pair (where M could be either Co or Fe; note that neighbors in the periodic table cannot be distinguished easily in EXAFS measurements). However, based on points (i) and (ii) mentioned above, M is most likely Co; and in the structure shown in Fig. 1a, the FeN_3 and CoN_3 coordination moieties all have a comparable M–N bond length of *ca.* 2 Å. However, this structure does not provide an explanation for the peak near 2.4 Å, as the distance from Fe to the N atoms bonded to Co is 3.4 Å. To obtain a Fe–N distance near 2.4 Å, the Co–N vertical bonds in Fig. 1a are tilted towards Fe by 30°, as shown in Fig. 3d (the atomic positions of this cluster are provided in the Table S7†).

Using the cluster structure depicted in Fig. 3d, theoretical EXAFS functions for Fe–N and Fe–Co were calculated using FEFF7 (phase shifts were included in the calculations).[23] The data were then fitted to a sum of five peaks: three Fe–N peaks (for N atoms N_1, N_2, and N_3), one Fe–Co peak for the Co neighbour, and one multi-scattering (MS) peak involving scattering from Fe to N_2 to N_3 to Fe. In these fits, the number of neighbors was fixed according to the model and only the pair distance and pair distribution width (σ) varied for each peak. The distance for the MS peak is sensitive to the configuration of N atoms about Fe. The sum of the three Fe–N EXAFS functions fit the broad peak very well including the shoulder near 1.9 Å, while the Fe–Co function models the 2nd main peak (Fig. 3c). The fitting results are summarized in Table S8.† The MS peak is quite small but did not shift much from the starting value, indicating that the relative positions of N_2 and N_3 are close to that in Fig. 3d.

These results are consistent with an N_3Fe–CoN_3 structure as depicted in Fig. 3d, where the FeN_3 and CoN_3 moieties are on mutually orthogonal planes, with a direct Fe–Co bonding linkage and a tilted N–Co bond. The synergistic interaction arising from the dual metal sites can reduce the free energy of the rate-determining step in ORR/OER, leading to enhanced electrocatalytic activity, as observed below.[13,20,24]

ORR electrocatalysis

The ORR activity and durability were then examined by CV measurements in O_2-saturated 0.1 M KOH at the potential scan rate of 50 mV s^{-1} (solid curves, Fig. 4a). The NCAG/Fe–Co sample shows a cathodic peak at +0.881 V, close to that of NCAG/Fe (+0.885 V) but much higher than that of NCAG/Co (+0.817 V). Further insights were acquired in linear sweep voltammetry (LSV) measurements with a rotating (ring) disk electrode (RDE/RRDE). One can see that all samples apparently outperformed commercial Pt/C, and NCAG/Fe–Co stood out as the best among the series. For instance, the onset potential (E_{onset}) and half-wave potential ($E_{1/2}$) were estimated to be +1.04 V and +0.89 V for NCAG/Fe–Co, +1.01 V and +0.89 V for

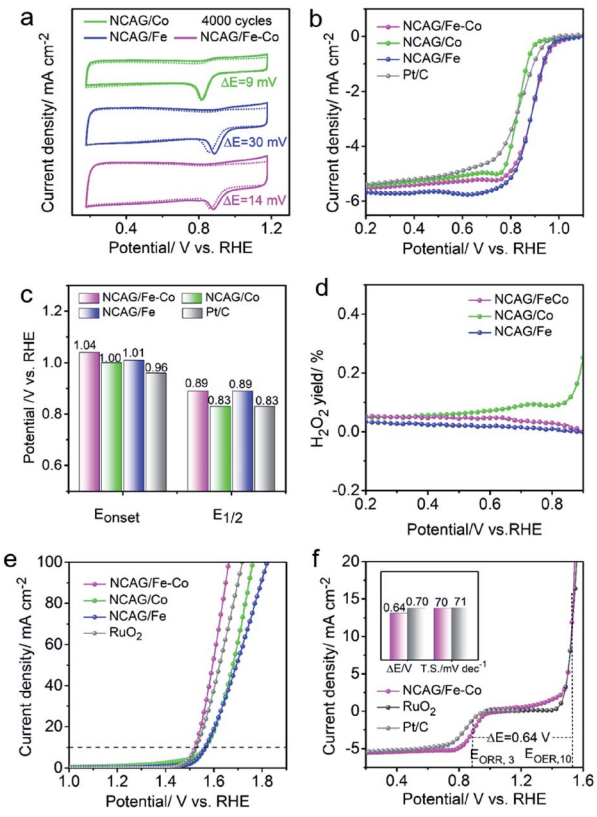

Fig. 4 (a) CV curves of the various catalysts before (solid curves) and after (dotted curves) 4000 cycles in O_2-saturated 0.1 M KOH (scan rate: 50 mV s^{-1}). (b) LSV curves of the various ORR catalysts at 1600 rpm and 5 mV s^{-1}. (c) E_{onset} and $E_{1/2}$ of the various catalysts. (d) H_2O_2 yield of the various catalysts. (e) OER polarization curves of the various catalysts. (f) Combined polarization curves of oxygen electrocatalysis of NCAG/Fe–Co and Pt/C–RuO_2. Inset shows the corresponding ΔE's and Tafel slopes.

NCAG/Fe, +1.00 V and +0.83 V for NCAG/Co, as compared to +0.96 V and +0.83 V for Pt/C (Fig. 4b and c). The kinetic current density (J_k) at the potential of +0.85 V shows a similar variation, 8.5 mA cm^{-2} for NCAG/Fe–Co, 8.9 mA cm^{-2} for NCAG/Fe, and 2.1 mA cm^{-2} for NCAG/Co, highlighting the unique ORR activity of Fe SACs (Fig. S6†). In addition, RRDE studies showed that the NCAG/Fe–Co sample produced a low H_2O_2 yield of 0.1% within a wide potential range from +0.2 V to +0.9 V, indicating four-electron reduction of oxygen (Fig. 4d and S7†).

In addition to the excellent activity towards ORR, NCAG/Fe–Co also displayed good stability. As shown in Fig. 4a, after 4000 continuous potential cycles (dotted curves), the CV peak exhibited only a negative shift of 14 mV, which is close to that of NCAG/Co (9 mV), but much lower than that of NCAG/Fe (30 mV). The NCAG/Fe–Co also exhibited a better ORR activity in acid than NCAG/Fe and NCAG/Co (Fig. S8†).

Taken together, these results show that the incorporation of Co into the NCAG/Fe aerogel nanocomposite leads to marked enhancement of both the ORR activity and durability, most likely due to the synergistic interactions between the Fe and Co centers, as manifested in XPS and EXAFS measurements (Fig. 2 and 3).

OER electrocatalysis and flexible Zn–air battery

As reversible oxygen catalytic activity is necessary for a rechargeable metal–air battery, the obtained carbon aerogels were then deposited onto carbon paper to examine the OER performance in 1 M KOH. Fig. 4e depicts the OER polarization curves. One can see that to reach the anodic current density of 10 mA cm^{-2}, the required overpotential ($\eta_{OER,10}$) was only +293 mV for NCAG/Fe–Co, very close to that of commercial RuO_2 (+297 mV), but markedly lower than those of NCAG/Co (+336 mV) and NCAG/Fe (+335 mV), demonstrating the unique advantage of the synergistic interaction between Fe and Co that boosted the OER activity in NCAG/Fe–Co.[8] The corresponding Tafel slope for NCAG/Fe–Co is estimated to be 70 mV dec^{-1}, close to that of RuO_2 (71 mV dec^{-1}), again, revealing favorable OER kinetics (Fig. 4f inset).

Generally, the overall reversible ORR/OER catalytic activity is evaluated by the potential gap (ΔE) between the ORR potential at 3 mA cm^{-2} ($E_{ORR,3}$) and OER potential at 10 mA cm^{-2} ($E_{OER,10}$). Thanks to the excellent ORR and OER activity, NCAG/Fe–Co affords a small ΔE of only 0.64 V, 60 mV lower than that (0.70 V) with commercial Pt/C and RuO_2 as the ORR and OER catalysts, respectively (Fig. 4f and inset).

In view of the excellent reversible ORR/OER catalytic performance of the NCAG/Fe–Co aerogels, a rechargeable Zn–air battery was assembled using the NCAG/Fe–Co as the oxygen catalysts, and the performance was compared to that based on a mixture of commercial Pt/C–RuO_2 catalysts (mass ratio = 1 : 1). As shown in Fig. S8,† the liquid Zn–air batteries assembled with NCAG/Fe–Co and Pt/C–RuO_2 display an open circuit voltage (OCV) of 1.51 V and 1.44 V, respectively, manifesting excellent practicability of the dual-metal carbon aerogels as oxygen catalysts. When a PAM hydrogel was employed as the solid electrolyte to assemble a solid Zn–air battery instead of a KOH solution (Fig. 5a and b), the NCAG/Fe–Co solid battery can be observed to show an OCV of 1.47 V and a maximum power density of 117 mW cm^{-2}, about 110 mV and 25 mW cm^{-2} higher than those based on commercial Pt/C–RuO_2 catalysts, and markedly better than most leading results with relevant catalysts reported in the literature (Table S9†).[25–31] After 1000 cycles of discharge–charge tests, the NCAG/Fe–Co solid battery exhibited a much smaller discharge–charge voltage gap, indicating its excellent rechargeability (Fig. 5c). Significantly, when the PAM thickness was compressed by 20% and 60%, the solid battery can still retain 96% and 92% of the maximum power density (Fig. 5b). In addition, this solid-state device exhibited a high OCV of about 1.47 V when bended at 120° to 180° (Fig. 5d). These compression and bending experiments indicate good flexibility of the NCAG/Fe–Co solid battery. It is notable that only two NCAG/Fe–Co solid batteries are needed in series to light up 10 LEDs with a rated voltage of about 3.0 V, indicating great potential for practical applications.

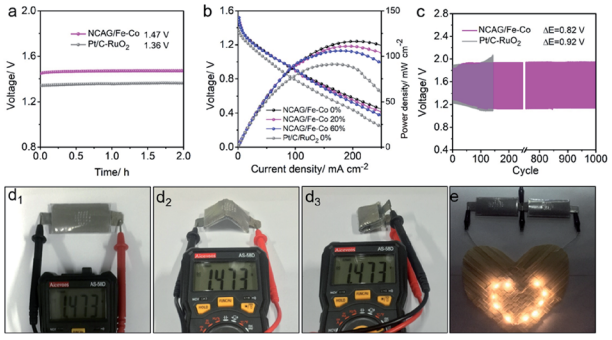

Fig. 5 (a) Open circuit voltage of a solid Zn–air battery with NCAG/Fe–Co as the oxygen electrode catalysts, in comparison to that with a mixture of commercial Pt/C–RuO_2 (mass ratio 1 : 1). (b) Discharge polarization and corresponding power density curves at 0%, 20%, and 60% compressive strains with a PAM hydrogel as the electrolyte. (c) Long-term cycling performance of the solid Zn–air batteries at 5 mA cm^{-2} with NCAG/Fe–Co and Pt/C–RuO_2 as the oxygen electrode catalysts. (d) Photographs of the solid Zn–air battery with NCAG/Fe–Co as the oxygen electrode catalysts showing an open-circuit voltage of 1.473 V under various bending conditions. (e) Photograph of two solid Zn–air batteries connected in series lighting up 10 LEDs, with NCAG/Fe–Co as the oxygen electrode catalysts.

Conclusions

In this study, carbon aerogels with atomic dispersion of Fe–Co dual sites (NCAG/Fe–Co) were prepared by controlled pyrolysis of a hydrogel precursor. HRTEM and elemental mapping analysis revealed homogeneous distributions of the metal sites within the defected carbon lattices. XPS measurements suggested electron transfer from the Fe to Co sites and the metal centers were mostly involved in MN_3 coordination. Consistent results were obtained in XAS measurements, where the FeN_3 and CoN_3 moieties were arranged in an orthogonal configuration, with a direct Fe–Co bonding interaction. Such a unique structure was found to facilitate the electrocatalysis of both ORR and OER. Electrochemically, the NCAG/Fe–Co nanocomposites exhibited an apparent electrocatalytic activity towards both ORR

and OER, with a performance superior to leading results of relevant catalysts reported in the literature. The bifunctional electrocatalytic activity and stability was also found to be markedly enhanced, as compared to the monometal counterparts, with a small ORR/OER potential gap (ΔE) of 0.64 V, 60 mV lower than that (0.70 V) with commercial Pt/C and RuO_2 catalysts. When NCAG/Fe–Co was used as the oxygen electrode catalysts for a Zn–air battery with either a liquid or solid electrolyte, the device showed a drastically better performance than that based on a mixture of commercial Pt/C–RuO_2, in terms of OCV, maximum power density, and rechargeability. Notably, the solid-state Zn–air battery exhibited excellent retention of the performance under various compressions and bendings, suggesting great potential as a flexible power device. Taken together, results from this study open up an ingenious pathway in the rational design and engineering of highly efficient and durable oxygen electrocatalysts based on dual metal-doped carbon aerogels for flexible metal–air batteries.

Conflicts of interest

There are no conflicts to declare.

Acknowledgements

Y. Z. acknowledged support from the National Natural Science Foundation of China (21972169, 21773311). Y. C. acknowledged support from the Fundamental Research Funds for the Central Universities of Central South University. The authors thank Kang Liu and Prof. Min Liu in Central South University for the assistance in the acquisition of the XANES and EXAFS data, and Yuyuan Zhang, Yong Wang in Central South University for helpful discussion. S. W. C. acknowledged support from the US National Science Foundation (CHE-1900235).

Notes and references

1 Q.-Q. Yan, D.-X. Wu, S.-Q. Chu, Z.-Q. Chen, Y. Lin, M.-X. Chen, J. Zhang, X.-J. Wu and H.-W. Liang, *Nat. Commun.*, 2019, **10**, 4977.
2 X. Zhao, X. Liu, B. Huang, P. Wang and Y. Pei, *J. Mater. Chem. A*, 2019, **7**, 24583–24593.
3 X. Lv, Y. Chen, Y. Wu, H. Wang, X. Wang, C. Wei, Z. Xiao, G. Yang and J. Jiang, *J. Mater. Chem. A*, 2019, **7**, 27089–27098.
4 B. Lu, L. Guo, F. Wu, Y. Peng, J. E. Lu, T. J. Smart, N. Wang, Y. Z. Finfrock, D. Morris, P. Zhang, N. Li, P. Gao, Y. Ping and S. Chen, *Nat. Commun.*, 2019, **10**, 631–642.
5 Y. Peng, B. Lu, L. Chen, N. Wang, J. E. Lu, Y. Ping and S. Chen, *J. Mater. Chem. A*, 2017, **5**, 18261–18269.
6 S. Zhu, J. Ge, C. Liu and W. Xing, *EnergyChem*, 2019, **1**, 100018.
7 L. Ma, S. Chen, Z. Pei, Y. Huang, G. Liang, F. Mo, Q. Yang, J. Su, Y. Gao, J. A. Zapien and C. Zhi, *ACS Nano*, 2018, **12**, 1949–1958.
8 J. Liu, T. He, Q. Wang, Z. Zhou, Y. Zhang, H. Wu, Q. Li, J. Zheng, Z. Sun, Y. Lei, J. Ma and Y. Zhang, *J. Mater. Chem. A*, 2019, **7**, 12451–12456.
9 Y. Wang, J. Hao, J. Yu, H. Yu, K. Wang, X. Yang, J. Li and W. Li, *J. Energy Chem.*, 2019, **45**, 119–125.
10 M. Chen, Y. He, J. S. Spendelow and G. Wu, *ACS Energy Lett.*, 2019, **4**, 1619–1633.
11 Y. Peng, B. Lu and S. Chen, *Adv. Mater.*, 2018, **30**, 1801995.
12 H. Shen, T. Thomas, R. Sefiu Abolaji, A. Saad, C. Hu and M. Yang, *Electrochem. Energy Rev.*, 2019, **2**, 252–276.
13 H. Fei, J. Dong, Y. Feng, C. S. Allen, C. Wan, B. Volosskiy, M. Li, Z. Zhao, Y. Wang, H. Sun, P. An, W. Chen, Z. Guo, C. Lee, D. Chen, I. Shakir, M. Liu, T. Hu, Y. Li, A. I. Kirkland, X. Duan and Y. Huang, *Nat. Catal.*, 2018, **1**, 63–72.
14 H. Xue, T. He, J. M. Chabu, J. Liu, H. Wu, J. Zheng, M. Tan, J. Ma, R. Shen, L. Deng and Y. Zhang, *Adv. Mater. Interfaces*, 2018, **5**, 1701345.
15 T. He, H. Xue, X. Wang, S. He, Y. Lei, Y. Zhang, R. Shen, Y. Zhang and J. Xiang, *Nanoscale*, 2017, **9**, 8341–8348.
16 W. Xie, Y. Song, S. Li, J. Li, Y. Yang, W. Liu, M. Shao and M. Wei, *Adv. Funct. Mater.*, 2019, **29**, 1906477.
17 H. Guo, Q. Feng, K. Xu, J. Xu, J. Zhu, C. Zhang and T. Liu, *Adv. Funct. Mater.*, 2019, **29**, 1903660.
18 W. Ren, X. Tan, W. Yang, C. Jia, S. Xu, K. Wang, S. C. Smith and C. Zhao, *Angew. Chem., Int. Ed.*, 2019, **58**, 6972–6976.
19 Y.-H. Wang, J.-B. Le, W.-Q. Li, J. Wei, P. M. Radjenovic, H. Zhang, X.-S. Zhou, J. Cheng, Z.-Q. Tian and J.-F. Li, *Angew. Chem.*, 2019, **131**, 16208–16212.
20 X. Han, X. Ling, D. Yu, D. Xie, L. Li, S. Peng, C. Zhong, N. Zhao, Y. Deng and W. Hu, *Adv. Mater.*, 2019, **31**, 1905622.
21 T. He, Y. Zhang, Y. Chen, Z. Zhang, H.-Y. Wang, Y. Hu, M. Liu, C.-W. Pao, J.-L. Chen, L.-Y. Chang, Z. Sun, J. Xiang, Y. Zhang and S. Chen, *J. Mater. Chem. A*, 2019, **7**, 20840–20846.
22 X. Fu, N. Li, B. Ren, G. Jiang, Y. Liu, F. M. Hassan, D. Su, J. Zhu, L. Yang, Z. Bai, Z. P. Cano, A. Yu and Z. Chen, *Adv. Energy Mater.*, 2018, **9**, 1803737.
23 A. L. Ankudinov and J. J. Rehr, *Phys. Rev. B: Condens. Matter Mater. Phys.*, 1997, **56**, 1712–1715.
24 J. Wang, Z. Huang, W. Liu, C. Chang, H. Tang, Z. Li, W. Chen, C. Jia, T. Yao, S. Wei, Y. Wu and Y. Li, *J. Am. Chem. Soc.*, 2017, **139**, 17281–17284.
25 J. Bian, X. Cheng, X. Meng, J. Wang, J. Zhou, S. Li, Y. Zhang and C. Sun, *ACS Appl. Energy Mater.*, 2019, **2**, 2296–2304.
26 Q. Xu, H. Jiang, Y. Li, D. Liang, Y. Hu and C. Li, *Appl. Catal., B*, 2019, **256**, 117893.
27 Z. Wang, J. Ang, B. Zhang, Y. Zhang, X. Y. D. Ma, T. Yan, J. Liu, B. Che, Y. Huang and X. Lu, *Appl. Catal., B*, 2019, **254**, 26–36.
28 X. Chen, B. Liu, C. Zhong, Z. Liu, J. Liu, L. Ma, Y. Deng, X. Han, T. Wu and W. Hu, *Adv. Energy Mater.*, 2017, **7**, 1700779.
29 C.-Y. Su, H. Cheng, W. Li, Z.-Q. Liu, N. Li, Z. Hou, F.-Q. Bai, H.-X. Zhang and T.-Y. Ma, *Adv. Energy Mater.*, 2017, **7**, 1602420.
30 D. Liu, B. Wang, H. Li, S. Huang, M. Liu, J. Wang, Q. Wang, J. Zhang and Y. Zhao, *Nano Energy*, 2019, **58**, 277–283.
31 D. Ji, L. Fan, L. Li, N. Mao, X. Qin, S. Peng and S. Ramakrishna, *Carbon*, 2019, **142**, 379–387.